Dynamics of prolate spheroids in the vicinity of an air–water interface

Stefano Villa, Domenico Larobina, Antonio Stocco, Christophe Blanc, Massimiliano Villone, Gaetano d'Avino, Maurizio Nobili

Soft Matter

ARTICLE TYPE

Cite this: DOI: 00.0000/xxxxxxxxxx

Dynamics of Ellipsoidal Particles in the Vicinity of an Air-Water Interface

Stefano Villa,[a] * Domenico Larobina,[b] Antonio Stocco,[c] Christophe Blanc,[d] Massimiliano M. Villone,[e] Gaetano D'Avino,[e] and Maurizio Nobil[d‡]

Received Date
Accepted Date

DOI: 00.0000/xxxxxxxxxx

We present the tracking of ellipsoidal micrometric particles close to an air-water interface performed with Dual Wave Reflection Interference Microscopy. Particle's position and angles with respect to the interface are simultaneously measured as a function of time. From the measured Mean Square Displacement five particle mobilities (3 translational and 2 rotational) and two translational-rotational cross-correlations are extracted and compared with our simulations, obtained imposing either slip and no-slip boundary conditions. The comparison reveals an agreement with no-slip boundary conditions prediction for orthogonal translation and out-of-plane rotation, and with slip ones for parallel translations and in-plane rotation. We rationalize these evidences in the framework of surface incompressibility at the interface.

1 Introduction

The dynamics of spherical particles dispersed in a Newtonian fluid near an interface has been widely studied in the past both experimentally and theoretically. Although for a fluid-fluid interface the particle dynamics is expected to be governed by slip boundary conditions (BC) [1–3], experiments often deviates from expectations. Indeed, while all experimental results relative to the movement parallel to the interface approaches predictions for full slip BC [4–6], for orthogonal dynamics the measured mobilities range from slip to no-slip BC [6–8]. Deviation from slip boundary condition has been recently rationalized considering the presence of small concentration of interfacial active agents determining surface incompressibility [8,6]. In this perspective, our group has shown that surface incompressibility at air-water interface peculiarly affects Brownian dynamics of spherical particles, with movement normal to the interface approaching no-slip BC predictions, while the one parallel being in agreement with full-slip BC [6].

Differently from spherical particles, the dynamics of colloids with complex morphology is still almost unexplored [9–13]. Earlier studies have mostly focused on ellipsoidal particles [14], as this morphology is the simplest after the spherical one. Because of anisotropy, particle hydrodynamic interactions with the confining interface result in a complex tensorial mobility, which demands the knowledge not only of the position but also of the orientation and the aspect ratio of the ellipsoid. Studies of ellipsoids in the presence of a fluid-fluid interface concerned mainly the absorption [15,16] and the 2D confined dynamics at the interface [17]. Very little is known on the dynamics of an ellipsoidal particle near an air-liquid interface. This lack of knowledge contrasts with the essential role played by the mobility of micrometric non-spherical entities close to fluid interfaces. Many systems of practical interest, like the motion of bacteria in biofilm formation [18,19], the draining dynamics in flotation processes [20], and the fabrication of Pickering emulsions [21], demand indeed the knowledge of the near interface particle mobilities.

In this paper, we study the dynamic behavior of micrometric ellipsoids near an air-water interface. Using Dual Wave Reflection Interference Microscopy (DW-RIM) [22], we are able to measure the dynamics of five (3 translational and 2 rotational) degrees of freedom of the particle, along with the particle aspect ratio and its distance from the interface. In particular, we here address how the surface incompressibility affects the ellipsoid rotational degrees of freedom and the translational-rotational cross correlations. The experimental results are compared with the outcomes of our numerical simulations.

[a] *Max Planck Institute for Dynamics and Self-Organization, 37077 Göttingen, Germany.*
[b] *Institute of Polymers, Composites, and Biomaterials, National Research Council of Italy, Naples, 80055 Portici, Italy.*
[c] *Institut Charles Sadron, CNRS UPR22, University of Strasbourg, Strasbourg, France.*
[d] *Laboratoire Charles Coulomb (L2C), UMR 5221 CNRS-Université de Montpellier, Montpellier, France.*
[d] *Department of Chemical, Materials and Production Engineering, University of Naples Federico II, P.le Tecchio 80, 80125 Naples, Italy.*
∗ E-mail: stefano.villa@ds.mpg.de
‡ E-mail: maurizio.nobili@umontpellier.fr

2 Materials and methods

2.1 Sample preparation and experimental set-up

Prolate ellipsoids are produced at the desired aspect ratio (A), i.e. the ratio between the major and the minor axes, in the range 5 to 12 by stretching with a custom developed stretching device sulfate latex beads of diameter $2a = 8.7 \pm 0.9$ μm (*MolecularProbes*^{TM}) embedded in a Poly(vinyl alcohol) matrix and heated at 100°C[23]. For each particle, we measure the time evolution of the three translation degrees of freedom (x, y, and z) together with the zenithal angle (θ), which the ellipsoid's major axis forms with the air-water interface plane xy, and the azimuthal angle (ϕ) of rotation of the major axis projection in the xy plane (see Fig. 1).

Samples are prepared dispersing ellipsoids in a cell made of a hollow glass cylinder enclosed on the top by a microscope slide and exposed to air on the bottom. Water pinning at the lower cylinder edges prevents water falling due to gravity. Ellipsoids number concentration is chosen low enough to allow neglecting inter-particles hydrodynamic couplings (mutual distance at the interface vicinity larger than 100 μm). Sample cell is then located on the sample stage of the DW-RIM set-up which, in brief, consists of a custom inverted microscope working in reflection and mounting a 50X long working distance objective*. The set-up is designed to simultaneously illuminate with two low coherence monochromatic light sources† and to collect the interference signal from the reflections at the particle-water and at the air-water interfaces with an RGB camera. The choice of an RGB camera is motivated by the exigence of simultaneously recording in different channels the light incoming from the two light sources. From the interference pattern information on the motion orthogonal to the interface is accessed, while the superposition of the two wavelengths allows to unequivocally determine the particle-interface distance[6,22]. All precautions are taken to reduce evaporation, vibrations and particles drifts[24]. Because of gravity, ellipsoids sediment towards the air-water interface until they reach an equilibrium gap distance at few hundreds of nanometers where gravity is balanced by DLVO repulsion[22]. At equilibrium, ellipsoids major axis is on average parallel to the interface, but because of thermal agitation θ fluctuates in a range of few degrees (less than 5°) around zero. After the equilibrium position is reached, data are acquired for few minutes at 30 fps in order to recover trajectories of 5000-10000 frames length.

2.2 Data acquisition and analysis

Dedicated algorithms have been designed specifically for the tracking of the DW-RIM interference pattern of ellipsoidal particles (Fig. 2). The distance z and the zenithal angle θ are collected analyzing, for each frame, the interference (see Fig. 2). Simultaneously, the movement in the plane parallel to the air-water interface along the axes parallel (x) and orthogonal (y) to the ellipsoid main axis and the azimuthal angle ϕ are accessed by tracking the interference pattern center of mass and its orientation (see Supplementary Information).

With this procedure the obtained resolutions are 100 nm for the ellipsoid x and y positions, few nanometers for z, 0.3° for ϕ and about 10% for θ. A more detailed description of the optical system and of experimental technique can be found in Ref.[22].

The data reported in the present work refer to 11 different ellipsoids with average aspect ratio 8.4 ± 1.9 and mean distance from the air-water interface in the range 787 ± 103 nm. In figure 3, typical time evolution of the measured positions (Fig. 3a) and orientations (Fig. 3b) is shown for one ellipsoid.

From the tracking the Mean Square Displacement (MSD) (Fig. 3c) and the Mean Square Angular Displacement (MSAD) (Fig. 3d) are evaluated: $MSD_k(\tau) = \left\langle [k(t+\tau) - k(t)]^2 \right\rangle_t$, where k is x, y, z, θ and ϕ (for notation simplicity in equations we name MSD_k both the MSD and the MSAD). From the MSD and MSAD the diffusion coefficient D_k along the freely diffusive degrees of freedom x, y and ϕ are obtained with a linear fit. As it can be seen in Figs. 3a and 3b, the motion along z and the rotation along θ are not free but confined in the DLVO potential due to the colloid and the air-water interface interactions[22]. As a consequence, MSD_z and MSD_θ are both characterize by sub-diffusive behavior with a plateau for large lag times. They are therefore fitted with the analytic solution of the Langevin equation assuming an harmonic potential[25,26], whose free fitting parameters are the diffusion coefficient and the potential stiffness. Translational and rotational mobilities M_k are obtained as $M_k = D_k/k_BT$, where k_B is the Boltzmann constant and T the temperature.

2.3 Simulations

Because of the lack of exact models for ellipsoids at close distance to the interface, we compare experimental results with numerical simulations. The latter are designed considering a free-buoyant

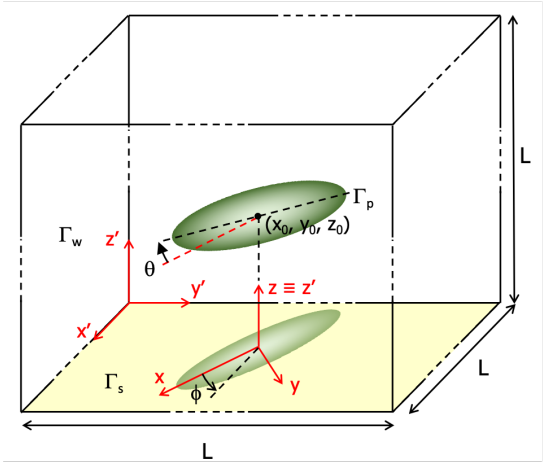

Fig. 1 Geometry of the system where measured and simulated parameters are reported:reference systems solidal to the laboratory (x',y',z') and to the ellipsoid (x,y,z), ellipsoid's center of mass coordinates (x_0,y_0,z_0), zenithal angle θ between ellipsoid major axis and x axis, azimuthal angle ϕ in the xy plane. The simulation is performed within a cube of lateral size L and with boundary surfaces Γ_p (particle surface), Γ_w (all the external boundaries of the computational domain except the air-water interface) and Γ_s (the air-water interface).

* Mitutoyo Apochromatic objective MY50X-805, 50X, WD 3, NA 0.55.
† *Thorlabs collimated LEDs* M625L3-C2 and M505L3-C2.

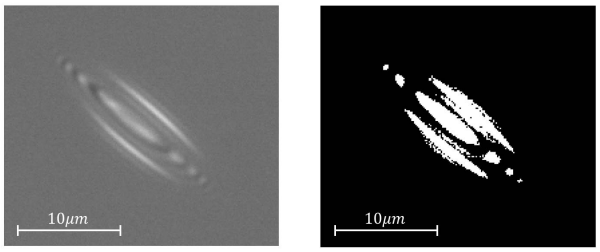

Fig. 2 Typical interference pattern of an ellipsoidal particle of aspect ratio 6 as it is recorded from the camera (a) and after binarization (b). Data relative to the red cannel. Please note that the high intensity lateral wings are not part of the interference pattern but consequences of multiple reflection and refraction inside the ellipsoid.

rigid ellipsoid suspended in an incompressible Newtonian liquid in proximity of an interface, where both full-slip ($v_\perp = 0$, $\partial_\perp v_\parallel = 0$) and no-slip ($v_\perp = 0$, $v_\parallel = 0$) BC are simulated ‡. Such

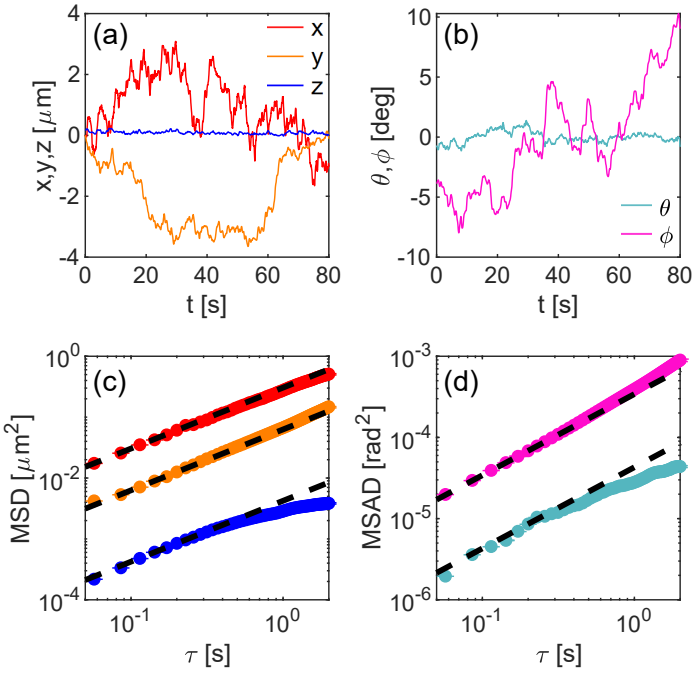

Fig. 3 Data relative to the trajectory of one of the tracked ellipsoids after sedimented to the air-water interface. a. Translational measured degrees of freedom x (red line), y (orange line) and z (blue line). b. Rotational measured degrees of freedom θ (light-blue line) and ϕ (magenta line). c. Mean Square Displacement along x, y and z (same colors of a). Dashed lines are linear guidelines representing the expected behaviour for a free Brownian diffusion. d. Mean Square Angular Displacement along ϕ and θ (same colors of b). Dashed lines are linear guidelines representing the expected behaviour for a free Brownian diffusion.

‡ In the boundary conditions expression, $\parallel$ and $\perp$ denote respectively the direction parallel and perpendicular to the interface, the velocities are the one of the fluid at the considered interface and $+$ and $-$ symbols represent the right and the left limit with respect to the position of the interface.

BC have been chosen based on previous results on the Brownian diffusion of spherical particles[6] where the surface incompressibility condition results in a no-slip BC for particle diffusion along the z-axis and quasi-slip BC for the parallel one. The same no-slip BC is expected to hold for an ellipsoid diffusing perpendicularly to an incompressible interface (see Supplementary Informations). On the ellipsoid surface, no-slip boundary conditions are imposed. A schematic representation of the investigated system is shown in Fig. 1. A Cartesian reference frame with the origin at the air-water interface and with the $z-$axis orthogonal to the interface is considered. The particle is positioned with its center of mass on the $z-$axis. The system of partial differential equations along with the BC are reported in the Supplementary Informations.

We solve the governing equations by applying a single non-zero component of the combined force/torque vector (F,T) and compute the six components of the translational and rotational velocity vector (u,ω). By varying the imposed non-zero component of the force/torque vector, in six iterations we can compute the full mobility matrix M[27]:

$$\begin{pmatrix} u \\ \omega \end{pmatrix} = M \cdot \begin{pmatrix} F \\ T \end{pmatrix} \tag{1}$$

that is symmetric and positive definite and can be partitioned as:

$$M = \begin{bmatrix} M_a & M_b \\ M_b^T & M_c \end{bmatrix} \tag{2}$$

with both the submatrices M_a and M_c being symmetric. The submatrices M_a and M_c account for the translational and rotational coupling, whereas M_b accounts for the translation-rotation coupling.

Due to the symmetry, for any particle-interface distance z, all the configurations obtained for different azimuthal angles ϕ (rotations around the $z-$axis) are equivalent. Consequently, the particle-interface hydrodynamic interactions and, in turn, the mobility matrix are functions of z and θ only, namely, $M = M(z,\theta)$. Because of the invariance for rotations around z-axis, it is sufficient to compute the mobility matrix only for configurations with the major axis of the spheroid lying in the xz-plane; the mobility or friction matrices for orientations outside the xz-plane are simply obtained by rotations around z-axis.

3 Results and Discussions

We compare the measured mobilities M_k^{meas} with simulations obtained using slip and no-slip BC M_k^{sim}. To this aim, for each experiment, we run a simulation having as input the measured values of a, b and average z for the particle at hand, with θ kept fixed to zero§. For the five mobilities we define the mobility relative difference as: $\Delta M_k/M_k^{sim} = (M_k^{meas} - M_k^{sim})/M_k^{sim}$. In Fig. 4a-c, we report $\Delta M_k/M_k^{sim}$ for the translational motion, in the case of slip (full circles) and no-slip (open circles) BC. The reported values

§ We checked that the experimental fluctuations in z around its mean value and of θ around 0° only slightly affect the simulated mobilities.

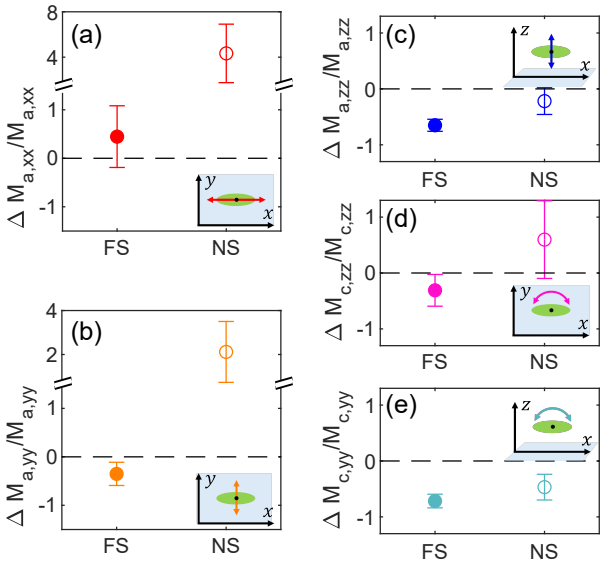

Fig. 4 Relative difference of mobilities between data and simulations for full slip (filled circles) and no-slip (empty circles) boundary conditions. The reported data refer to: (a) $M_{a,xx}$, (b) $M_{a,yy}$, (c) $M_{a,zz}$, (d) $M_{c,yy}$, (e) $M_{c,zz}$. In the corresponding insets, sketches depict the motion direction or the rotation with respect to the interface (laying on the xy plane).

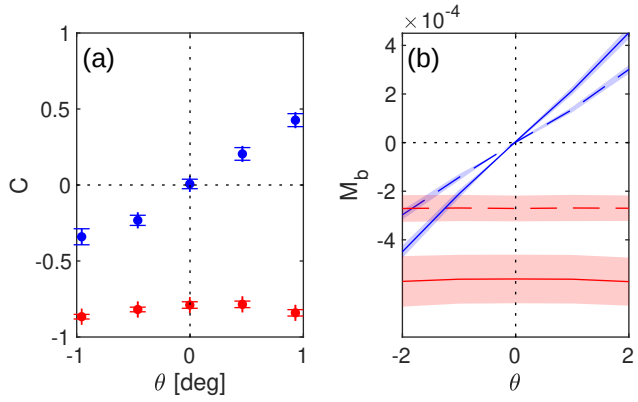

Fig. 5 a. Cross-correlations vs. theta: blue circles correspond to $C_{v_z,\omega}(\theta)$, red squares corresponds to $C_{v_x,\omega}(\theta)$. b. Cross mobilities $M_{b,zy}$ (blue) and $M_{b,xy}$ (red) vs. theta: full line represent simulation with slip BC, while dashed line the simulation with no-slip BC.

with their error bars represent the averages and standard deviations on the 11 measured particles. As expected the experimental translational mobilities parallel to the interface (Figs. 4a, 4b) are close to the slip BC, while the translational mobility orthogonal to the interface (Fig. 4c) approach the no-slip BC.

In Fig. 4d-e, we also report the in-plane and out-of-plane rotational mobility relative difference, again for slip (full circles) and no-slip (open circles) BC. Consistently with the translations, the average value of the in-plane rotational mobility (Fig. 4d) is close to slip BC, while the one of the out-of-plane rotational mobility is near to no-slip BC (Fig. 4e). Actually, in the case of the out-of-plane rotational mobility the two boundary conditions give comparable results within the experimental error. This is not surprising because, for small θ, the rotation is equivalent to the superposition of two orthogonal motions in opposite directions localized on the ellipsoid tips. In such an idealized picture, the interfacial velocity field has the symmetry of a dipolar field having both radial and non-radial components. Since slip BC applies for the non-radial component and no-slip BC for the radial one, we expect similar differences in both cases. Please note that for both BC the measured significant deviations from the simulated values can result from the large experimental noise on θ[¶].

We also evaluated the cross correlations between different degrees of freedom, comparing their trend with simulated cross mobilities. To this aim we calculate the rotational-translational cross-correlations $C_{v_z,\omega}$ and $C_{v_x,\omega}$ (at time delay 0) between the angular velocity of the out-of-plane rotations ω and two components of the particle velocity: v_z, along the interface normal, and v_x, along the ellipsoid main axis.

$$C_{v_i,\omega}(\theta) = \left. \frac{\langle v_i(\theta,t)\cdot\omega(\theta,t+\tau)\rangle_t}{\sqrt{\langle v_i^2(\theta,t)\rangle_t \cdot \langle \omega^2(\theta,t)\rangle_t}} \right|_{\tau=0} \quad (3)$$

In Eq. (3), v_i is either v_z or v_x and $\langle ... \rangle_t$ indicates the time average on t. Angular dependency is obtained splitting the trajectories in 5 different subsets depending on the instantaneous value of θ and evaluating Eq. (3) for each interval of θ. In Fig. 5a are reported the cross correlations averaged over all the measured ellipsoids, where the abscissa reports the average angle θ in each subset of data.

In the case of $C_{v_z,\omega}$ for negative θ we observe that v_z and ω are anti-correlated, while for positive θ they are correlated. To rationalize the observed cross-correlation, note that as soon as θ deviates from zero one extremum of the ellipsoid is farther from the interface than the other. In this condition, if the particle approaches the interface (negative v_z), the ellipsoid extremum closer to the interface will experience a greater drag, independently from the assumed BC. Consequently the ellipsoid is subjected to a torque restoring the condition $\theta = 0$. Therefore, if $\theta > 0$ a $v_z < 0$ induces an $\omega < 0$, while $v_z > 0$ induces an $\omega > 0$, and thus in both cases a positive cross correlation holds. Viceversa, if $\theta < 0$, a $v_z < 0$ induces an $\omega > 0$, while a $v_z > 0$ induces an $\omega < 0$, and thus in both cases a negative cross correlation. It is worth noticing that the observed cross correlation is not a consequence of the ellipsoids-interface potential well, which also tries to restore the $\theta = 0$ condition. Indeed, in the limit of a harmonic potential, a rotation of the ellipsoid along θ would generate only a restoring torque, with no force in the direction of the z axis.

For $C(v_x,\omega)$, the negative sign observed indicates that the behaviour is anti-correlated for both $\theta > 0$ and $\theta < 0$, as in systems where parallel drag decreases approaching the boundary[28].

In order to verify whether the cross-mobilities have the same trend as the cross-correlations, we simulated and reported in Fig. 5b the cross mobilities $M_{b,zy}$ (blue curves) and $M_{b,xy}$ (red curves) versus θ: where $M_{b,zy}$ corresponds to $C(v_z,\omega)$, while $M_{b,xy}$ cor-

¶ As error on θ propagates from the error on b (see Supplementary Information) an improved characterization of the ellipsoids semi-axes should be required for improving the measurement of θ.

responds to $C(v_x, \omega)$. For each mobility both no-slip (dashed line) and slip (continuous line) BC are considered. The cross-mobilities are simulated for an ellipsoid of aspect ratio $A = 8.6$ at a particle-interface distance $z_c/2b = 1.167$, corresponding to the average aspect ratio and distance of the experiments. Shadowed regions in Fig. 5b account for the inter-sample aspect ratio variance $\Delta A = \pm 0.6$.[||]

The trend of the simulated mobilities is the same of the experimental cross correlations, for both full-slip and no slip BC.

4 Conclusions

We report the first systematic study of mobilities of a micrometric ellipsoidal particle in the close vicinity of an air-water interface. Five different ellipsoidal mobilities (3 translational and 2 rotational) are measured and compared with dedicated simulations for slip and no-slip boundary conditions. Moreover, the out-of-plane and the in-plane roto-translations cross-correlations are calculated and compared with simulated cross-mobilites. Analogously to the spherical particles[6], surface incompressibility rules the translational mobilities: parallel ones approach predictions for slip BC, while the orthogonal one is close to no-slip BC. The rotational degrees of freedom reinforces the importance of surface incompressibility on the mobility of the ellipsoid: in fact, the in-plane rotation mobility is governed by the slip BC, while the one of out-of-plane rotation is controlled by the non-slip BC. The roto-traslations cross-correlations are found in a qualitatively agreement with the simulated cross-mobilites.

We believe that our findings will be relevant to predict the motion of micro and nano entities close to liquid interfaces in a variety of fields ranging from biophysics to material processing. In particular, the relevance of the present results can be perceived considering the strong geometrical analogy of the present system with the one of a living bacteria moving close to an air water interface. Indeed, recent papers report how anomalies on the motion of *Escherichia coli*[12] and *Pseudomonas aeruginosa*[29] results from surface incompressibility, thus making the classical theoretical assumption of free air-water interface far from reality in such systems. Pointing out the additional effect of surface incompressibility on the rotational dynamics, we hope to help systematize the study of surface incompressibility effects on the dynamics of micrometric organisms in water and stimulating further investigations in the field.

Notes and references

1 H. Brenner, *Chem. Eng. Sci.*, 1961, **16**, 242.

2 G. Perkins and R. Jones, *Physica A: Statistical Mechanics and its Applications*, 1991, **171**, 575.

3 A. V. Nguyen and G. M. Evans, *Journal of colloid and interface science*, 2004, **273**, 262–270.

4 G. M. Wang, R. Prabhakar and E. M. Sevick, *Phys. Rev. Lett.*, 2009, **103**, 248303.

5 S. Villa, G. Boniello, A. Stocco and M. Nobili, *Advances in Colloid and Interface Science*, 2020, **284**, 102262.

6 S. Villa, C. Blanc, A. Daddi-Moussa-Ider, A. Stocco and M. Nobili, *Journal of Colloid and Interface Science*, 2023, **629**, 917–927.

7 J. C. Benavides-Parra, D. Jacinto-Méndez, G. Brotons and M. D. Carbajal-Tinoco, *J. Chem. Phys.*, 2016, **145**, 114902.

8 A. Maali, R. Boisgard, H. Chraibi, Z. Zhang, H. Kellay and A. Würger, *Phys. Rev. Lett.*, 2017, **118**, 084501.

9 A. Chakrabarty, A. Konya, F. Wang, J. V. Selinger, K. Sun and Q.-H. Wei, *Phys. Rev. Lett.*, 2013, **111**, 160603.

10 S. Ota, T. Li, Y. Li, Z. Ye, A. Labno, X. Yin, M.-R. Alam and X. Zhang, *Phys. Rev. E*, 2014, **89**, 053010.

11 J. M. A. Paweł Czajka and M. Długosz, *ACS Omega*, 2019, **4**, 17016–17030.

12 S. Bianchi, V. C. Sosa, G. Vizsnyiczai and R. D. Leonardo, *Sci. Rep.*, 2020, **10**, 4609.

13 N. Shokeen and A. Mukhopadhyay, *Coll. Poly. Sci.*, 2021, **229**, 1595–1603.

14 Y. Han, A. M. Alsayed, M. Nobili, J. Zhang, T. C. Lubensky and A. G. Yodh, *Science*, 2006, **314**, 626–630.

15 S. Coertjens, R. D. Dier, P. Moldenaers, L. Isa and J. Vermant, *Langmuir*, 2017, **33**, 2689–2697.

16 A. Wang, W. B. Rogers and V. N. Manoharan, *Phys. Rev. Lett.*, 2017, **119**, 108004.

17 G. Boniello, C. Blanc, D. Fedorenko, M. Medfai, N. B. Mbarek, M. In, M. Gross, A. Stocco and M. Nobili, *Nature Material*, 2015, **14**, 908–911.

18 S. Bianchi, F. Saglimbeni, G. Frangipane, D. Dell'Arciprete and R. Di Leonardo, *Soft matter*, 2019, **15**, 3397–3406.

19 D. P. Rivas, N. D. Hedgecock, K. J. Stebe and R. L. Leheny, *Soft Matter*, 2021, **17**, 8195–8210.

20 Y. Xing, X. Gui, L. Pan, B.-E. Pinchasik, Y. Cao, J. Liu, M. Kappl and H.-J. Butt, *Adv. Coll. Interf. Sci.*, 2017, **246**, 105.

21 Y. Chevalier and M.-A. Bolzinger, *Coll. and Surf. A: Phys. and Eng.*, 2013, **439**, 23.

22 S. Villa, A. Stocco, C. Blanc and M. Nobili, *Soft Matter*, 2020, **16**, 960–969.

23 C. Ho, A. Keller, J. Odell and R. Ottewill, *Colloid Polym. Sci.*, 1993, **271**, 469–479.

24 V. Stefano, *PhD thesis*, Université de Montpellier, 2018.

25 M. C. Wang and G. E. Uhlenbeck, *Rev. Mod. Phys.*, 1945, **17**, 323–342.

26 S. K. T. Li, D. Medellin and M. G. Raizen, *Science*, 2010, **328**, 1673–1675.

27 J. Happel, *Low Reynolds number hydrodynamics: with special applications to particulate media*, Springer, 1983.

28 S. Lee and L. Leal, *Journal of Fluid Mechanics*, 1980, **98**, 193–224.

29 J. Deng, M. Molaei, N. G. Chisholm and K. J. Stebe, *arXiv preprint arXiv:2204.02300*, 2022.

|| In the experimental ranges, simulations are more sensitive to the aspect ratio than to particle-interface distance.